Mapping forest successional stages in the Brazilian Amazon using forest heights derived from TanDEM-X SAR interferometry

Polyanna Da Conceição Bispo[a,b,*], Matteo Pardini[c], Konstantinos P. Papathanassiou[c], Florian Kugler[c], Heiko Balzter[a,b], Dominik Rains[d,e], João Roberto dos Santos[f], Igor G. Rizaev[g], Kevin Tansey[a], Maiza Nara dos Santos[h], Luciana Spinelli Araujo[i]

[a] Leicester Institute for Space and Earth Observation, Centre for Landscape and Climate Research, School of Geography, Geology and Environment, University of Leicester, Leicester, United Kingdom
[b] NERC, National Centre for Earth Observation at the University of Leicester, Leicester, United Kingdom
[c] German Aerospace Center (DLR), Microwave and Radar Institute, Oberpfaffenhofen, Wessling, Germany
[d] Department of Environment, Ghent University, Ghent, Belgium
[e] Earth Observation Science, Department of Physics & Astronomy, University of Leicester, Leicester, United Kingdom
[f] Remote Sensing Division, National Institute for Space Research (INPE), São José dos Campos, Brazil
[g] Visual Information Laboratory, University of Bristol, Bristol, United Kingdom
[h] Embrapa Agricultural Informatics, Brazilian Agricultural Research Corporation (Embrapa), Campinas, SP, Brazil
[i] Embrapa Environment, Brazilian Agricultural Research Corporation (Embrapa), Jaguariúna, SP, Brazil

ARTICLE INFO

ABSTRACT

Knowledge of the spatial patterns of successional stages (i.e., primary and secondary forest) in tropical forests allows to monitor forest preservation, mortality and regeneration in relation to natural and anthropogenic disturbances. Different successional stages have also different capabilities of re-establishing carbon stocks. Therefore, a successful discrimination of successional stages over wide areas can lead to an improved quantification of above ground biomass and carbon stocks. The reduction of the mapping uncertainties is especially a challenge due to high heterogeneity of the tropical vegetation. In this framework, the development of innovative remote sensing approaches is required. Forests (top) height (and its spatial distribution) are an important structural parameter that can be used to differentiate between different successional stages, and can be provided by Interferometric Synthetic Aperture Radar (InSAR) acquisitions. In this context, this paper investigates the potential of forest heights estimated from TanDEM-X InSAR data and a LiDAR digital terrain model (DTM) for separating successional stages (primary or old growth and secondary forest at different stages of succession) by means of a maximum likelihood classification. The study was carried out in the region of the Tapajós National Forest (Pará, Brazil) in the Amazon biome. The forest heights for three years (2012, 2013 and 2016) were estimated from a single-polarization in bistatic mode using InSAR model-based inversion techniques aided by the LiDAR digital terrain model. The validation of the TanDEM-X forest heights with independent LiDAR H100 datasets was carried out in the location of seven field inventory plots (measuring 50 × 50 m, equivalent to 0.25 ha), also allowing for the validation of the LiDAR datasets against the field data. The validation of the estimated heights showed a high correlation (r = 0.93) and a low uncertainty (RMSE = 3 m). The information about the successional stages and forest heights from field datasets was used to select training samples in the LiDAR and TanDEM-X forest heights to classify successional stages with a maximum likelihood classifier. The identification of different stages of forest succession based on TanDEM-X forest heights was possible with an overall accuracy of about 80%.

1. Introduction

Many tropical forest regions are a mosaic made up of large areas of primary forest and degraded forest patches, the latter for example created by logging, fire or timber harvesting. The degraded forest patches can be at different successional stages of regeneration and are

referred to as secondary forests (Chokkalingam and De Jong, 2001; Nyirambangutse et al., 2017). The primary forest can be defined as a forest that preserves its original condition (Chokkalingam and De Jong, 2001) and it is the most biodiverse forest type characterized by a full and dense canopy top and several layers of understory. The ground layer is generally clear of dense vegetation because the canopy layer allows very little light to penetrate. In secondary forests, the lack of a full canopy results in more light reaching the ground layer allowing for dense ground vegetation. The secondary forests play an important role in the structural and functional maintenance of biodiversity in the ecosystem (Vieira and Gardner, 2012) and have the capability of re-establishing carbon stocks and the nutrient cycling properties of the primary forests or old growth forests (Vieira et al., 2003). Depending on the length of regeneration and its history in terms of land-use, a secondary forest can be classified into three different successional stages (Mesquita et al., 2001; Araújo et al., 2005; Chazdon et al., 2007; Salomão et al., 2012), namely initial, intermediate and advanced stages. These stages are characterized by different forest structure patterns and species compositions (Lu et al., 2003; Chazdon et al., 2007; Silva et al., 2016).

Due to their large-scale mapping capabilities, (space borne) remote sensing systems play a critical role in acquiring information about the spatial distribution of successional stages across wide areas, especially in tropical forests that are in general difficult to access from the ground, despite optical remote sensing systems being limited by the presence of clouds in these areas. Lu (2005) for example have integrated inventory data and Landsat TM images to classify secondary forests in the Brazilian Amazon in initial, intermediate and advanced stages reaching an overall accuracy of 80%. A different approach using multi-temporal Landsat images was followed by Espírito-Santo et al. (2005) mapping forest successional stages after deforestation in the Tapajós National Forests (Brazilian Amazon) reaching a classification accuracy of 73%. As an alternative to using optical systems, Synthetic Aperture Radar (SAR) data overcomes the limitations imposed by cloud cover. Using such data, primary and secondary forests at different successional stages could be discriminated in the Brazilian Amazon reaching an overall accuracy of about 80% (Santos et al., 2003; Martins et al., 2016; Pavanelli et al., 2018). However, when either using optical or SAR data, in most studies the clear separation of the intermediate successional stages, in between the initial and advanced stages (Santos et al., 2003; Galvão et al., 2009; Martins et al., 2016; Pavanelli et al., 2018), is particularly challenging. Martins et al. (2016) analysed different stages of forests affected by fires in the northern Amazon (Brazil) using ALOS PALSAR data by relating changes in the PALSAR signal (coherent and incoherent metrics) to above ground biomass (AGB) and different successional stages of forests affected by fires. Although the full polarimetric L-band PALSAR data were sensitive to variations in forest structure, they were not able to discriminate between the intermediate levels of forest degradation or regeneration. Rare are studies using height or variations in height to identify forest successional stages in tropical areas. Berveglieri et al. (2016), for instance, discriminated between the successional stages based on local height variations provided by a digital surface model (DSM) derived from optical images (historical and present). The study was developed in a semi-deciduous tropical forest fragment located in the west of São Paulo State, Brazil. The successional stages could be identified and compared over time using a time series of imagery and DSMs, allowing to identify forest cover changes. Aslan et al. (2018) investigated the use of ALOS Prism data for detecting mangrove succession through canopy height estimation in Mimika Papua, Indonesia and Sundarbans, Bangladesh. They used the ALOS Global Digital Surface Model World (AW3D30) DSM dataset acquired between 2006 and 2011 to map canopy heights at different successional stages of mangroves and were able to differentiate the variability of canopy height estimates between an intact mangrove and a severely degraded mangrove ecosystem.

According to Lu et al., 2003, the knowledge of parameters, such as tree height, age, above ground biomass, and diameter at breast height (DBH) provide a way to characterize and separate tropical forest stands at different successional stages. However, an accurate knowledge of height is especially critical, since in most of the ecosystems there is a high correlation between the height and the AGB, DBH and basal area (BA) (Feldpausch et al., 2011; Feldpausch et al., 2012; Banin et al., 2012). None of these parameters can be measured directly at single tree level by any remote sensing configurations. However, Light Detection and Ranging (LiDAR) and Interferometric or Polarimetric-Interferometric SAR (InSAR/Pol-InSAR) configurations can provide estimates of the top height of the vegetation volume for a given resolution on the ground. The potentials of InSAR/Pol-InSAR techniques to estimate forest top height have been demonstrated in several experiments (Cloude and Papathanassiou, 2003; Cloude et al., 2013; Garestier et al., 2008; Askne et al., 1997). Over forest scenes, InSAR/Pol-InSAR techniques face some limitations because most spaceborne InSAR/Pol-InSAR data available are acquired in repeat-pass mode, and therefore are affected by temporal decorrelation (Zebker and Villasenor, 1992; Lee et al., 2009), resulting in inaccurate height estimates. In 2010, the German Aerospace Center (DLR) TanDEM-X mission became operative. TanDEM-X is a single-pass InSAR system that provides bistatic X-band data (~3 cm wavelength) without temporal decorrelation and with global coverage. The potential of TanDEM-X bistatic InSAR data for estimating forest height, biomass, and characterizing forest changes over time has been evaluated in several studies (Caicoya et al., 2016; Kugler et al., 2014; Schlund et al., 2015; Treuhaft et al., 2015; Næsset et al., 2016; Treuhaft et al., 2017; Lei et al., 2018) in boreal, temperate, and tropical forests. However, X-band has a lower capability to penetrate forest canopy compared to longer wavelengths like L-band. Several authors (Khati et al., 2017; Khati et al., 2018; Kugler et al., 2014; Schlund et al., 2014; Schlund et al., 2015) showed that X-band penetration depends on forest (e.g. dense or less dense forest), season (e.g. with or without leafs) or weather conditions (e.g. frozen or non-frozen). In those cases where penetration through to the ground is not given, an accurate inversion for forest height at X-band can still be achieved by using an a-priori known digital terrain model (Hajnsek et al., 2009; Kugler et al., 2014).

While several studies have been developed using TanDEM-X information applied to tree height and AGB estimation, few investigations have been carried out to separate tropical forest into different types or successional stages and to monitor their changes over time. In these studies, the TanDEM-X complex InSAR coherence or the digital elevation models (DEM) extracted from the phase centre height are typically used. Schlund et al. (2014) investigated the information content of bistatic TanDEM-X datasets for mapping forest and land cover classes in tropical peatlands. The results showed that the interferometric coherence improves the discrimination of thematic classes considerably compared to the monostatic datasets. The coherence and textural information from the bistatic mode for the classification of forest (closed canopy), forest (open canopy), grassland, shrubland, wetlands and water bodies resulted in an accuracy of about 85%. De Grandi and Mitchard (2016) tested the potential of TanDEM-X coherence and LiDAR observations to characterize structural heterogeneity based on one-point statistics in a tropical forest in East Kalimantan, Indonesia. They tested the discrimination between four land cover classes (primary forest, secondary forest, mixed scrub and grassland) but were unable to separate primary forest (or old-growth forest) from secondary forest using direct information from coherence or phase from TanDEM-X. Jeffries-Matusita (JM) separability was high between forest classes (primary and secondary) and non-forest (grassland) while primary and secondary forests were not separable. At the same study site, De Grandi et al. (2016) used the phase height information from TanDEM-X interferometry and airborne LiDAR DEMs to detect differences in vegetation heterogeneity through a disturbance gradient. They used two-point statistics (wavelet variance and covariance) to assess the dominant spatial frequencies associated with either topographic features or

canopy structure. Treuhaft et al., 2017 demonstrated the capability of radar-interferometric phase-height time series at X-band (wavelength = 3 cm) in old growth forest and secondary forests to monitor changes in vertical structure and AGB in the Tapajós National Forest, Brazil, with sub-hectare and monthly spatial and temporal resolution, respectively.

Different to the above-mentioned studies, in this paper the potential of forest top height estimated from TanDEM-X single-pass data for separating different successional stages is investigated for the first time. The experiments were carried out over the region of the Tapajós National Forest (Pará, Brazil) in the Amazon biome. The forest heights were estimated from single-polarization TanDEM-X data sets acquired in bistatic mode using an InSAR model-based inversion technique aided by the LiDAR digital terrain model (DTM). The separation of the forest stands into different successional stages has been formalized as a maximum-likelihood classification problem in which each class corresponds to a successional stage, and the different classes/successional stages are characterized by a distribution of estimated heights. Assuming this distribution to be Gaussian, the mean height and the height variance of each class have been estimated from a set of training samples.

This paper is organized as follows. Section 2 describes the study area and the datasets. TanDEM-X data have been used to estimate forest heights, LiDAR datasets were used to validate the estimated heights, and field datasets were used to identify locations of forest stands in the different successional stages for both the initialization of the maximum likelihood classifier, using heights from TanDEM-X, as well as the estimation of the accuracy of the classification results. The methodology applied to the estimation of forest heights, their validation, the successional stage classification and the estimation of its accuracy are reported in Section 3. The results are presented in Sections 4 and 5. Finally, Section 6 draws the conclusions of the study.

2. Study area and datasets

2.1. Study area

The study area is located on the eastern edge of the Tapajós National

Forest region (TNF) (Pará State, Brazil), as shown in Fig. 1. The climate of the region is classified by Köppen as *Ami*, with an average annual temperature of 25° C and an average relative humidity of 85%. The average annual rainfall is 1909 mm with a dry season ($< 100\,mm\,month^{-1}$) between July and November (Vieira et al., 2003). The site is situated in a relatively flat area with an elevation between 80 m and 180 m. The soils are nutrient-poor oxisols and ultisols with low pH, organic matter, and cation exchange capacity, and a high concentration of aluminium oxides (Silver et al., 2000). The vegetation of the TNF is composed of a continuous canopy of perennial trees with heights between 25 and 30 m and occasional emergent trees that reach up to 50–60 m height. This type of forest has several layers and sublayers under the canopy, including small trees, shrubby and herbaceous plants. Tall trees are approximately evenly spaced due to the low light penetration into the canopy. There are high amounts of climbing plants, especially epiphytes and lianas that often hide the outline of the trees (Ricklefs and Relyea, 2008).

The study site (black rectangles in Fig. 1(c)) was part of the TNF conservation until its exclusion in 2012 (law 12.678 in 2012 (Brasil, 2012)). Since then, land cover change in this area has increased significantly as a result of logging and other anthropogenic actions but also due to the abandonment of land allowing forest regeneration in some areas. As a result, the study site is covered by ombrophilous dense forest with old-growth or primary forest (abbreviated with OF or PF) and several stages of secondary succession forest (initial, SFIni, intermediate, SFInt, and advanced, SFAdv), crops/pasture and bare soil (non-forest). The vegetation structure for the successional stages is shown schematically in Fig. 2.

Table 1 shows the general characteristics of the successional stages shown in Fig. 2 based on studies collected and reviewed by Lu (2005) in the eastern (Altamira, Bragantina and Ponta de Pedras) and western (Rondonia) Brazilian Amazon (Moran and Brondizio, 1998; Lu et al., 2003). The TNF region is also part of the eastern Brazilian Amazon and has the same characteristics reported by Lu (2005). This is corroborated by local knowledge, the experience of the authors of this study and by other studies, for example Espírito-Santo et al. (2005), Silva et al. (2016), Bispo et al. (2016), Pôssa et al. (2018), Wiederkehr et al. (2019). The seven field plots used within this study, which include the

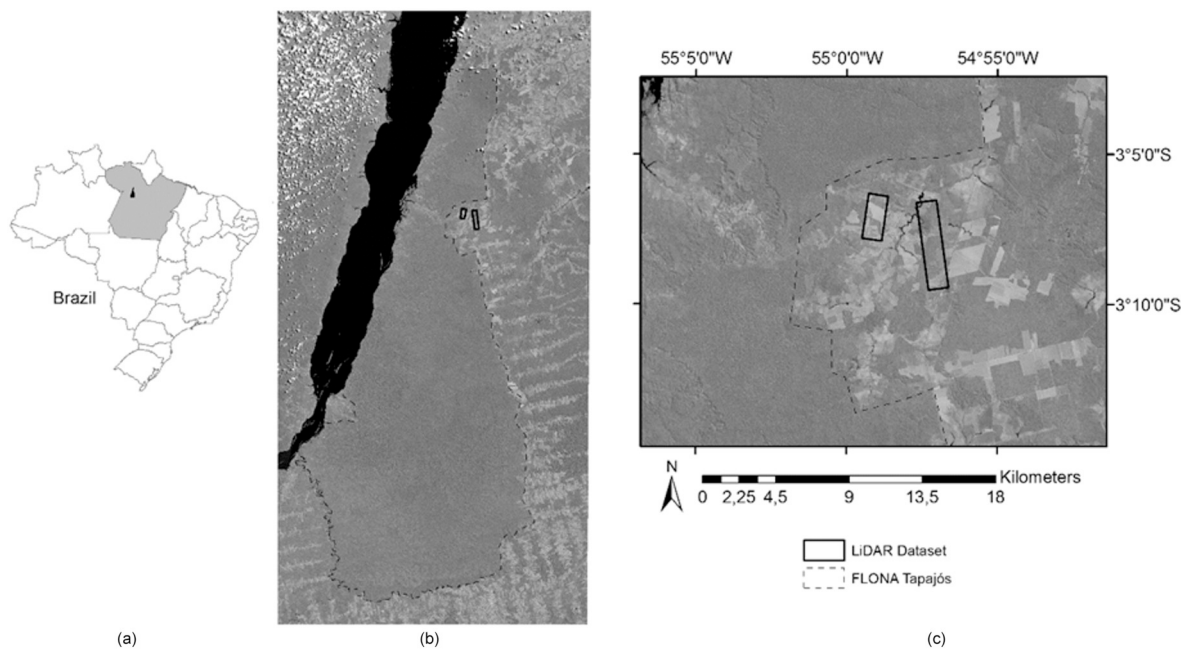**Fig. 1.** (a) Location of the TNF in the Brazilian territory. (b) Zoom on the TNF, enclosed by the dashed line (TNF limits from 2013). The two small rectangles delimit the area covered by the LiDAR acquisition. (c) Zoom on the LiDAR coverage. The whole area inside and outside of the two LiDAR rectangles is covered by each TanDEM-X acquisition used in this study (2012, 2013 and 2016). Background image: Landsat 8 (14/08/2015).
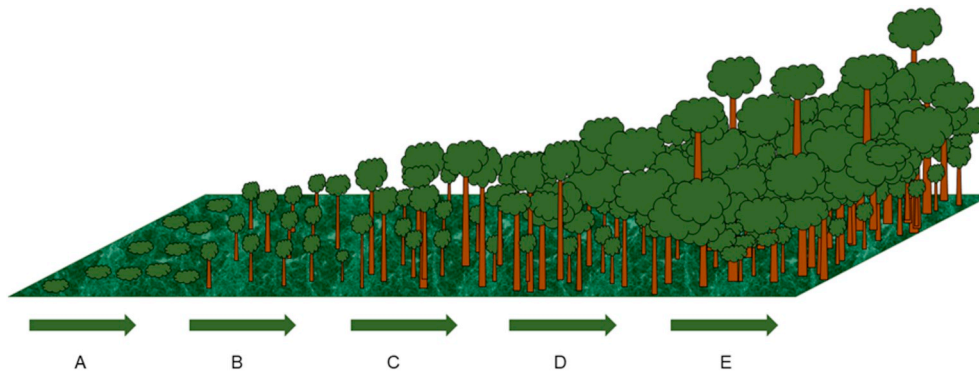
Fig. 2. Schematic representation of a tropical forest with different successional stages: A (non-forest); B (secondary forest in initial stage - SFIni); C (secondary forest in intermediated stage - SFInt); D (secondary forest in advanced stage - SFAdv): E (old growth forest or primary forest - OF).

same information as presented in Table 1, further confirm this (see Table 4).

2.2. Remote sensing data

Three dual-polarized interferometric TanDEM-X image pairs acquired in 2012, 2013 and 2016 were used. The images were acquired in bistatic mode, in ascending orbit with an average incidence angle of about 40°. The effective baselines of the three datasets varied between 80 m and 110 m. Table 2 summarizes the main characteristics of these acquisitions.

In addition, airborne LiDAR acquisitions taken in the same years as the TanDEM-X data sets, i.e. 2012, 2013 and 2016, are used in this study. Table 3 summarizes the characteristics of the LiDAR instruments. The LiDAR coverage is represented by the two rectangular areas shown in Fig. 1(c), with a total coverage of around 1011 ha. In 2012 and 2013 the LiDAR data were collected by Geoid Laser Mapping Ltd. (Belo Horizonte, Brazil) and in 2016 by SAI Serviços Aéreos Industriais (São Paulo, Brazil). The canopy height model (CHM), the height surface above the ground topography corresponding to the first LiDAR returns, was generated by means of standard LiDAR data processing algorithms using the Fusion software (McGaughey, 2014). The LiDAR data are publicly available at https://www.paisagensLiDAR.cnptia.embrapa.br/webgis/.

2.3. Reference data

The reference datasets are divided into three groups. The first group contains the LiDAR H100 data sets used for the validation of the forest heights estimated from TanDEM-X data. The H100 is a standard forestry canopy height measure and corresponds well to radar forest-height estimates, as it the top height of the volume (Hajnsek et al., 2009; Kugler et al., 2014). Details on its calculation are reported in Section 3.2.

The second group includes the field plot inventory collected in July and August 2013 used to validate the LiDAR canopy heights on which the H100 is based on. The field inventory data were obtained for twelve 0.25 ha plots (50 × 50 m) resulting in a total sample area of 3 ha, including 1813 individual trees belonging to 202 species and 49 plant families. The four corners of each plot were geolocated using differential Global Navigation Satellite Systems (GeoXH6000, Trimble Navigation, Ltd.), and the position of each stem was mapped with respect to the plot corner. Plot measurements included live trees, live palms and standing dead trees. In areas of old-growth forest, all individual trees with a diameter at breast height (DBH) equal to or larger than 10 cm were measured. In the secondary forest areas, the minimum DBH was 5 cm. However, only seven (about 700 trees) out of twelve

plots were actually used for the validation of the LiDAR canopy heights (Table 4).

Five inventory plots were excluded from the LiDAR canopy height validation as the majority of the tree positions within these plots were erroneously geolocated. Fig. 3 shows as an example how we verified the accuracy of the geographic positions and the heights of the individual trees within each plot. The tree crowns from the LiDAR canopy heights were visually compared to the crowns (circles with height attribute) measured in the field (Fig. 3). Although the original field measurement of the crowns include both x and y axes (major and minor axes) of each tree, the average of the two axes was used both for x and y for reasons of simplicity, thus representing the crowns as circles instead of ellipsoids.

In our study the locations of the 700 trees from the seven accurate plots of the field inventory data were also used to extract the corresponding pixel values of the LiDAR H100 and TanDEM-X interferometric heights for 2012, 2013 and 2016 for the validation of the TanDEM-X heights (see Section 4.1 for the results).

However, for the validation of the classification of the successional stages using the heights retrieved from the TanDEM-X 2012 and 2013 images, all of the twelve plots, which include information on the successional stage of the entire plot, were used for the validation of the classification, since for this purpose the position of the individual trees was not required.

The third group includes the data for the training and validation of the classification of the forest into different successional stages for 2012, 2013 and 2016. A total of 47,711 pixels were selected as training data for 2012 and 2013 based on field knowledge of the authors, local knowledge and studies developed by Bispo et al., 2014, Bispo et al., 2016 and Silva et al. (2016) (Table 5, Fig. 4). 14,787 pixels, which included also the pixels from the location of the twelve plots from 2013 taken in the field, as mentioned above, were used to validate the classification for 2012 and 2013. All the samples used for training and validation were located in areas where no significant changes occurred between 2012 and 2013. For 2016, a total of 15,388 pixels were selected as training samples, again based on field knowledge of the authors, local knowledge and studies developed by Bispo et al. (2014), Bispo et al. (2016), Silva et al. (2016), Pôssa et al. (2018) and Wiederkehr et al. (2019) (Table 6, Fig. 5). A total of 5,310 pixels were used for the validation of the forest succession classification for 2016 (Table 6, Fig. 5), which included pixels from the location of nine field inventory plots from 2015 (https://www.paisagensLiDAR.cnptia.embrapa.br/webgis/) and five additional plots obtained from the field work carried out in September 2016 as well as based on researcher knowledge. Details about the classification method and the validation are given in Section 3.3.

Table 1
General characteristics of forests types representative for the area of the TNF (which is part of eastern Amazon region) collected by Lu (2005). DBH, H, AGB and Age represent the interval of the means of stand diameter (cm), stand height (m), aboveground biomass (kg/m²) and age (years) respectively.

Forest types	Characteristics	DBH (cm)	H (m)	AGB (kg/m²)	Age (years)
SFIni	Herbaceous plants, seedlings, and saplings together are responsible for > 90% of total biomass. The vertical structure is characterized by a full profile of saplings and herbaceous plants. Saplings are the main structure element and represent the majority of the aboveground biomass.	2–5	2–6	0.5–5	1–5
SFInt	Saplings still account for most of the biomass in SFInt. Vegetation structure provides a mix of dense ground cover of saplings and young trees with higher canopy than SFIni. There is very small internal difference between canopy and understory individuals. SFInt is characterized by a lack of stratification between canopy and understory.	5–15	6–12	4–10	4–15
SFAdv	Trees occupy the canopy and present obvious stratification of forest stand structure in SFAdv. In this stage, there is a major shift in structure that differentiates understory from canopy individuals; that is, the presence of saplings is less significant than that of trees. One can find differences between the canopy and understory in terms of height and density of individuals at both levels.	10–25	9–17	8–25	10–50
OF or PF	In the mature forest, aboveground biomass and vegetation density can be considerably different depending on soil conditions, species composition, and topography at the site. In a typical mature forest, trees account for the majority of aboveground biomass, reaching > 90%. Many tree individuals are taller than 17 m, and some are between 25 m and 30 m, followed by a few scattered individuals over 35 m tall or emergent.	13–30 or more	11–25 or more	12–50	–

3. Methods

3.1. Estimation of forest heights from TanDEM-X data

In an interferometric acquisition, the observable relating the SAR data to the forest physical structure is the interferometric coherence. Focusing on the range - azimuth plane, let S_1 and S_2 be the (complex) amplitudes of two single-look complex images acquired in the same polarimetric channel from two orbits spatially separated by the interferometric baseline, i.e. at the two ends of the interferometer. For a fixed pixel, the complex InSAR coherence is defined as (Bamler and Hartl, 1998):

$$\gamma(\kappa_Z) = \frac{E\{S_1 S_2^*\}}{\sqrt{E\{|S_1|^2\} E\{|S_2|^2\}}} \tag{1}$$

where $E\{\}$ denotes the statistical expectation operator. Notice that in (1) the dependence on the range – azimuth coordinate has been dropped for notation simplicity, however the dependence of the coherence on the baseline through the vertical InSAR wavenumber κ_Z has been explicitly included on the left-hand side. κ_Z expresses the sensitivity (i.e., the derivative) of the phase difference between the two acquisitions with respect to the height in the volume. For bistatic acquisitions (like the TanDEM-X ones) it is defined as (Bamler and Hartl, 1998):

$$\kappa_Z = \frac{2\pi}{\lambda} \frac{\Delta\theta}{\sin\theta_0} \approx \frac{2\pi}{\lambda} \frac{B_\perp}{R \sin\theta_0} \tag{2}$$

where θ_0 is the nominal incidence angle, λ is the wavelength, $\Delta\theta$ the change of incidence angle induced by the perpendicular baseline $B_\perp$, and R the slant range distance. The so-called interferometric height of ambiguity (HoA) is the height difference that causes a 2π phase difference, and is given by HoA = $2\pi/\kappa_Z$. By assuming the spatial ergodicity of the scattering process, the coherence in (1) is normally estimated by substituting the statistical expectation with the average of neighbouring pixel amplitudes in a (multilook) cell around the pixel under consideration.

After filtering out the shift of the reflectivity spectra along the range caused by the different incidence angles (Zebker and Villasenor, 1992; Bamler and Hartl, 1998), the interferometric coherence $\gamma(\kappa_Z)$ can be decomposed into several contributions (Zebker and Villasenor, 1992):

$$\gamma(\kappa_Z) = \gamma_{Temp} \gamma_{Sys} \gamma_{Vol}(\kappa_Z) \tag{3}$$

$\gamma_{Vol}(\kappa_Z)$ is the so-called volume coherence. It depends on the geometric and dielectric characteristics of the forest volume, and is available after the non-volume coherence contributions γ_{Temp} and γ_{Sys} are compensated. γ_{Temp} is the temporal decorrelation caused by changes in time of the scene. It depends on the temporal stability of the scatterers, the temporal baseline of the interferometric acquisition and the dynamic environmental processes (e.g., action of wind, change of water content due to rain or seasonality, droughts, vegetation growths, etc.) occurring in the time between the acquisitions. For TanDEM-X bistatic acquisitions it can be considered as $\gamma_{Temp} = 1$ (Kugler et al., 2014). γ_{Sys} includes all the system-induced interferometric decorrelation effects. In the TanDEM-X case, the main contribution to γ_{Sys} is the one coming from the presence of additive white noise in the received radar signal. By using the noise equivalent sigma zero (NESZ) range – azimuth patterns provided along with the TanDEM-X data, the signal-to-noise ratio (SNR) can be estimated. Finally, based on the white thermal noise assumption, the SNR-related decorrelation can be calculated and compensated from $\gamma(\kappa_Z)$ (Kugler et al., 2014). Other systematic contributions due to residual processing inaccuracies can be estimated for instance by considering the highest coherence values in the scene (e.g. on bare surface areas) and then be compensated.

$\gamma_{Vol}(\kappa_Z)$ is linked to the vertical density of the received power (i.e. including backscattering and attenuation phenomena) $F(z)$ by means of

Table 2
Acquisition parameters of TanDEM-X. HoA indicates the InSAR height of ambiguity (see Section 3.1).

Date	Mode	Polarization	Orbit	Incidence Angle (°)	Effective Baseline (m)	HoA (m)
05/12/2012	Bistatic/StripMap	Dual (HH, VV)	Ascending	40.60	110.44	60.65
30/05/2013	Bistatic/StripMap	Dual (HH, VV)	Ascending	40.56	83.38	80.67
23/01/2016	Bistatic/StripMap	Dual (HH, VV)	Ascending	40.56	102.00	65.41

the following normalised Fourier relationship (Zebker and Villasenor, 1992), (Bamler and Hartl, 1998):

$$\gamma_{Vol}(\kappa_Z) = \frac{\int_{z_0}^{z_0+H_V} F(z)\exp\{j\kappa_Z z\}dz}{\int_{z_0}^{z_0+H_V} F(z)dz} \tag{4}$$

z_0 is the ground height, and H_V is the volume extension above z_0. $F(z)$ is also called vertical reflectivity profile.

The inversion of volume parameters from (4) needs a parameterization of $F(z)$ by means of a model. The model must contain enough physical structure to interpret the interferometric measurements, and at the same time it must be simple in terms of the number of parameters in order to be determinable with the available number of measured coherences. A two-layer model composed by the superposition of ground and volume scattering has been considered in several studies, see e.g. Treuhaft and Siqueira (2000), Papathanassiou and Cloude (2001), Kugler et al. (2014), and it is retained also here. If the scattering from the two layers is assumed to be statistically independent, it results in:

$$F(z) = F_G(z) + F_V(z) \tag{5}$$

where $F_G(z)$ and $F_V(z)$ represent the ground- and vegetation-only contributions to the global vertical reflectivity profile. $F_G(z)$ and $F_V(z)$ are related to the ground- and vegetation-only coherences $\gamma_G(\kappa_Z)$ and $\gamma_V(\kappa_Z)$, respectively, by means of a relationship formally equivalent to the one in (4). Further, as typically done, see e.g. Treuhaft and Siqueira (2000), Papathanassiou and Cloude (2001), Kugler et al. (2014), it is assumed that the ground reflectivity is described by a Dirac-δ function centered around the ground height z_0, representing surface and dihedral scattering contributions. The volume decorrelation term can be finally written as in Treuhaft and Siqueira (2000), Papathanassiou and Cloude (2001) and Kugler et al. (2014):

$$\gamma_{Vol}(\kappa_Z) = e^{j\kappa_Z z_0}\frac{\mu + \gamma_V(\kappa_Z)}{1 + \mu} \tag{6}$$

where μ is the effective ground-to-volume amplitude ratio specifying the influence of the ground. Finally, the modelling is completed by introducing a convenient parameterization of $F_V(z)$ that can characterize the related coherence $\gamma_V(\kappa_Z)$ well enough with a few parameters to enable an accurate forest height inversion even from a single interferometric baseline. A widely used model shapes $F_V(z)$ based on a uniform distribution of scatterers with constant backscattered power within the full volume extension and with constant extinction (Papathanassiou and Cloude, 2001; Kugler et al., 2014; Olesk et al., 2015):

Table 4
Field data from forest plots (0.25 ha) used as reference data. For H, DBH, Age and AGB the mean and the standard deviation (SD) is given with H being the stand height, DBH the diameter at breast height and AGB the aboveground biomass.

N. of Plots	Forest Types	H (m)		DBH (cm)		Age (years)		AGB (kg/m²)	
		Mean	SD	Mean	SD	Mean	SD	Mean	SD
1	SFIni	5	1.2	5	1.8	5	2	0.5	0.1
2	SFInt	9	0.8	10	3.0	15	1	4	0.8
3	SFAdv	14	2.1	19	2.0	30	1	17	1.2
1	OF	19	3.6	21	2.2	> 50	–	29	1.4

$$F_V(z) = e^{-2(H_V-z)\sigma/\cos\theta_0}, \text{ for } 0 \le z \le H_V \tag{7}$$

where σ is the (mean) extinction value, which defines the attenuation rate of the vegetation layer and fixes the shape of the exponential. The inversion of the forest height H_V based on Eqs. (6) and (7) from (polarimetric-) interferometric data has been demonstrated to lead to height estimates with 10–20% error in a wide range of boreal, temperate and tropical forest types at multiple wavelengths considering both airborne and space borne platforms, see Papathanassiou and Cloude (2001), Qi and Dubayah (2016), Sadeghi et al. (2016), Olesk et al. (2015), Soja et al. (2018), Lagomasino et al. (2016), Lee et al. (2013), Kugler et al. (2015), Hajnsek et al. (2009), provided that all non-volume decorrelation contributions have been well compensated and a sensitive (polarimetric-) interferometric observation space was available (Lee et al., 2013; Kugler et al., 2015).

With reference to the specific TanDEM-X case, the forest height H_V has to be estimated from a single interferometric bistatic acquisition in most of the cases. Eqs. (6) and (7) describe $\gamma_{Vol}(\kappa_Z)$ by means of four unknown parameters, i.e. z_0, H_V, μ and σ (Cloude and Papathanassiou, 2003). Thus, a balanced inversion problem between a number of observables and the unknown terms has to be established (Cloude and Papathanassiou, 2003; Treuhaft et al., 1996). In the single-baseline case, one way to balance the inversion is to consider at least two polarization channels assuming that $F_V(z)$ does not vary with polarization (Random Volume hypothesis). Here the only polarization dependent parameters is the ground-to-volume ratio μ. Dual-pol acquisitions like the ones available in Tapajós could then be suitable for implementing a polarimetric-interferometric inversion as described in (Kugler et al., 2014) after polarization optimization (Cloude and Papathanassiou, 1998). However, the dense forest stands of Tapajós are not assumed to provide enough penetration to the ground at X-band, therefore enough polarization diversity (thus a diversity of μ) to allow for a determined inversion, i.e. a unique solution in the estimation of H_V.

Table 3
Acquisition parameters of the LiDAR data.

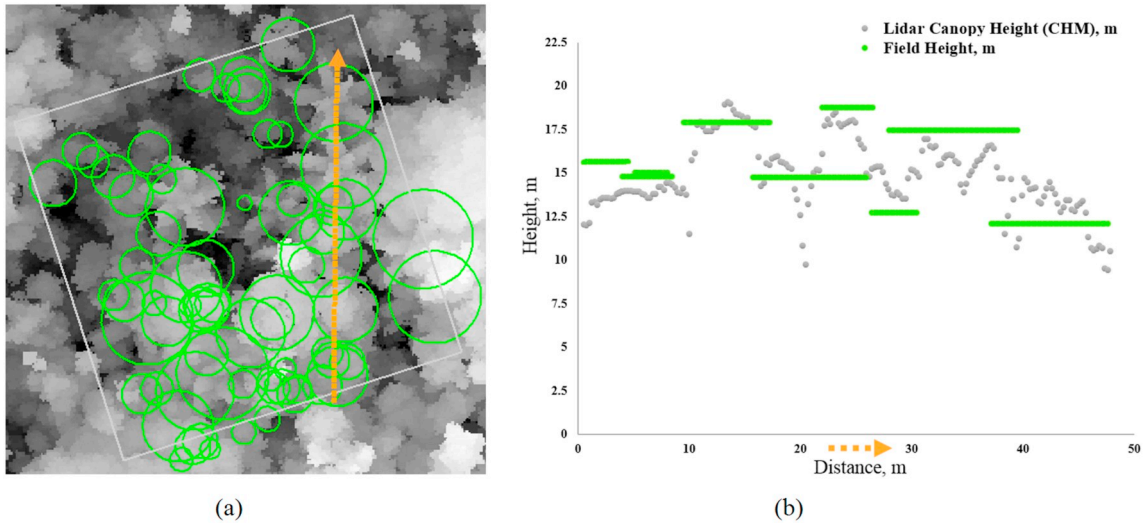| LIDAR	Acquisition date	Flight height	Field of view	Average return density	Total area	Scanner specification
Area 1	31/07/2012	850 m	11.1°	36.9 ppm²*	340 ha	ALTM 3100
	10/09/2013	853.4 m	11°	29.95 ppm²		OPTECH, ORION
	23/03/2016	700 m	15°	26.9 ppm²		OPTECH/ ALTM 3100
Area 2	30/07/2012	850 m	11.1°	38.9 ppm²*	671 ha	ALTM 3100
	10/09/2013	853.4 m	11°	29.95 ppm²		OPTECH, ORION
	22/03/2016	700 m	15°	26.09 ppm²		OPTECH/ ALTM 3100

Fig. 3. Example of the crowns of the trees (a) measured in the field for one plot of secondary forest in advanced stage, here represented as green circles superimposed over the LiDAR canopy heights (plot size: 50 × 50 m, grey box). The vertical profile of a transect (b) crossing the crowns and the LiDAR canopy heights. The position of the transect is shown as an orange arrow in subfigure (a).

Table 5
Classes and number of pixels selected for the classification of 2012 and 2013. Each pixel corresponds to 10 m².

Forest types	N. pixels for training	N. pixels for test
NF	9469	2950
SFIni	9116	2948
SFInt	9845	2985
SFAdv	9579	2959
OF	9702	2945

Table 6
Classes and number of pixels selected for the 2016 classification. Each pixel corresponds to 10 m².

Forest types	N. pixels for training	N. pixels for tests
NF	3087	1130
SFIni	2961	1044
SFInt	3196	1032
SFAdv	3136	1083
OF	3008	1021

Therefore, the inversion must rely on single-baseline, single-polarization interferometric data. One way to tackle the inversion is by using an a-priori known ground elevation model providing z_0. From Eqs. (6) and (7), other assumptions have to be made to further reduce the number of unknowns and to get a balanced and determined inversion. Here we retained $\mu = 0$. The LiDAR digital terrain model (DTM) has been used as z_0, resulting in a considerable reduction of the coverage of the height estimates from the coverage of the TanDEM-X acquisition to the coverage of the LiDAR acquisition (see Fig. 1). Phase offset trends linear in range

and in azimuth between the interferometric phase are associated to the LiDAR ground $\exp(j\kappa_Z z_0)$ and the estimated volume coherence phase have been compensated by exploiting ground control points in bare areas with high cohrence (larger than 0.9). Finally, H_V and σ have been estimated by means of the following least-squares fitting:

$$\widehat{H}_V, \hat{\sigma} = \underset{H_V, \sigma}{\operatorname{argmin}} \parallel \hat{\gamma}_{vol} \exp(-j\kappa_Z z_0) - \gamma_V(\kappa_Z; H_V, \sigma) \parallel^2 \tag{8}$$

where $\gamma_V(\kappa_Z; H_V, \sigma)$ is the modelled volume coherence from (6) and (7) after setting $\mu = 0$, and $\hat{\gamma}$ is the volume coherence estimated from the
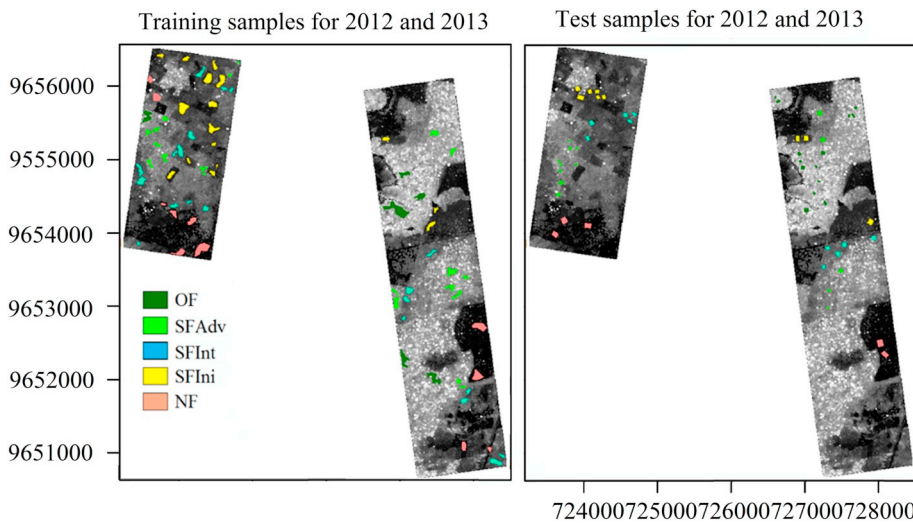

Training samples for 2012 and 2013   Test samples for 2012 and 2013

Fig. 4. Location of training samples and test samples used for the supervised classification and the validation sets for 2012 and 2013. The two rectangles correspond to the areas covered by the LiDAR acquisitions. The LiDAR H100 is shown as the grayscale background, and the location of training and test samples are the superimposed colored areas.
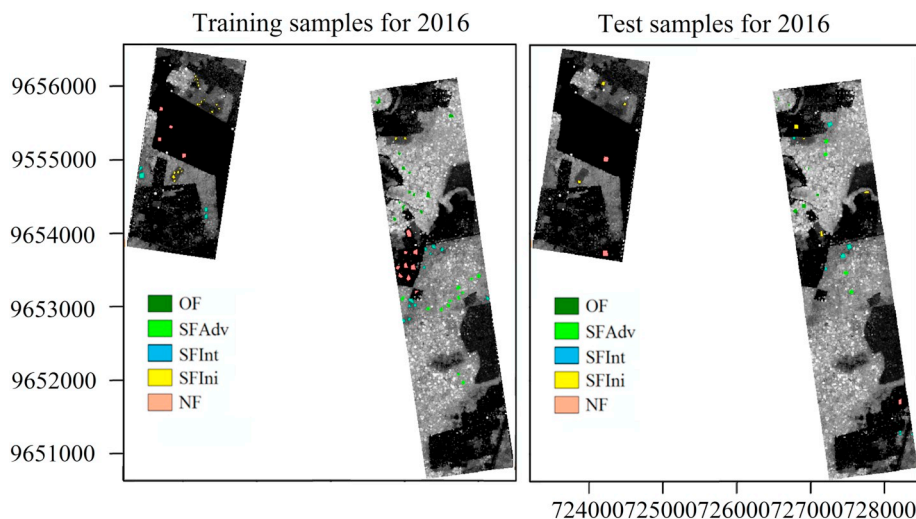
Fig. 5. Location of training samples and test samples used in the supervised classification and validation for 2016. The two rectangles correspond to the areas covered by the LiDAR acquisitions. The LiDAR H100 is shown as the grayscale background, and the location of training and test samples are the superimposed colored areas.

data after the compensation of the phase offset and of the non-volumetric decorrelation contributions. The minimization of the distance in (8) can be implemented on both the real and the imaginary part of the coherences, therefore providing two equations for *dual-pol* mode, one for each polarization, for the estimation of the unknowns H_V and σ. Notice that if $|\hat{\gamma}|$ is lower than 0.3, no inversion is carried out as it is assumed to be ill-conditioned due to the low value of the observed coherence.

3.2. Calculation of H100

The seven plots (corresponding to 700 tree locations) from 2013 were used to validate the LiDAR CHM of 2013 by taking the maximum CHM height for each separated crown.

The H100 heights were calculated from the LiDAR CHM of 2012, 2013 and 2016. The H100 is a forestry standard canopy top height measure, and it expresses the height of the considered vegetation volume (Van Laar and Akça, 2007; Hajnsek et al., 2009; Kugler et al., 2014). It has been calculated by taking the maximum of the LiDAR CHM heights within a moving window measuring 10 × 10 m.

It is worth stressing that the calculation of the H100 from a high resolution LiDAR CHM provides a height measure comparable to the radar one (Hajnsek et al., 2009). Otherwise, a CHM would provide heights lower than or equal to the radar ones, due to the sampling of the single crowns, especially for very small LiDAR beams.

The H100 heights at the 700 tree location of the seven inventory plots were used to validate the InSAR TanDEM-X forest heights.

3.3. Separation of successional stages using a supervised classification based on TanDEM-X forest heights

After their validation, the TanDEM-X heights based on the 2012, 2013 and 2016 acquisitions were used to discriminate between the different successional stages. This discrimination process has been formalized as a classification problem in which each class corresponds to a different successional stage, i.e. OF, SFAdv, SFInt and SFIni. The "non-forest" (NF) class was considered as well, resulting in a total of five classes. Additionally, the classification was applied to the LiDAR H100 heights for comparison.

A supervised maximum likelihood (ML) classifier (Richards and Xiuping, 2006) was separately carried out using either the TanDEM-X or LiDAR H100 heights as input. The areas used as training sets (heights) of all the five successional stage classes have been chosen based on previous studies (Bispo et al., 2014; Silva et al., 2016; Pôssa et al., 2018; Wiederkehr et al., 2019) and field visits. The classes, based

on field inventory measurements, are described in detail in Section 2.3. For 2012 and 2013 training areas were selected where no change in classes occurred between those two years. In 2016 the authors conducted field work where they also visually identified some of the forest classes. Additionally, we used the ground measurements of 2015 from the Landscape Sustainable project (https://www.paisagensLiDAR.cnptia.embrapa.br/webgis/) as test samples for estimating the accuracy achieved in the classification. The total number of pixels for the training and test samples are reported in Tables 5 and 6, and their locations are plotted in Fig. 4 and Fig. 5.

In the training phase of the ML classification algorithm, we assumed that the TanDEM-X or LiDAR H100 heights (the input of the classifier) are Gaussian distributed within each class:

$$f(H \mid \mu, \sigma^2) = \frac{1}{\sqrt{2\pi\sigma^2}} e^{-\frac{(H-\mu)^2}{2\sigma^2}} \tag{9}$$

Their unknown mean μ and variance σ^2 have been estimated from the training data (Richards and Xiuping, 2006).

Subsequently, pixels which are not part of the training data can be assigned to the class which they most likely belong to based on their height. The a posteriori distribution $P(i|H)$, i.e. the probability that a pixel with height H belongs to the i-th class, $i = 1, \dots, 5$, is given by:

$$P(i \mid H) = \frac{P(H \mid i)P(i)}{P(H)} \tag{10}$$

where $P(H|i)$ is the likelihood function (linked to the distribution of heights) in the i-th class, $P(i)$ is the probability that the i-th class occurs in the study area, and $P(H)$ is the probability that the height H occurs in the study area:

$$P(H) = \sum_{i=1}^{5} P(H \mid i)P(i) \tag{11}$$

Table 7
Interpretation of Kappa values.

Values of K	Interpretation
< 0	No agreement
0–0.19	Poor agreement
0.20–0.39	Fair agreement
0.40–0.59	Moderate agreement
0.60–0.79	Substantial agreement
0.80–1.00	Almost perfect agreement

Fig. 6. Interferometric heights derived from TanDEM-X (top panel) and H100 (bottom panel) derived from LiDAR CHM, for 2012, 2013 and 2016. For each year and sensor, the two rectangles correspond to the LiDAR coverage.

The generic height H is assigned to the i-th class by the rule:

$$H \in i \quad \text{if} \quad P(i \mid H) > P(j \mid H) \quad \text{for all} \quad j \neq i$$

which is equivalent to say that each pixel is assigned to the class with the highest likelihood.

The accuracy of the ML classification has been evaluated by first computing the confusion matrix. The dimension of the confusion matrix equals the number of classes, i.e. 5×5 elements in this case. The generic element C_{ij} in the i-th row and j-th column of the confusion matrix is calculated as:

$$C_{ij} = \text{number of pixels in the class } j \text{ attributed to the class } i$$

The elements of the diagonal of the confusion matrix represent the correctly assigned pixels. The classification performance has then been judged by means of the overall accuracy OA, which is the total percentage of pixels correctly classified (Richards and Xiuping, 2006):

$$OA = \frac{\sum\limits_{i=1}^{5} C_{ii}}{N} \times 100\% \tag{12}$$

where N is the total number of pixels. We also considered the Kappa coefficient K, which includes the off-diagonal elements as well as the diagonal terms to provide a more robust assessment of accuracy than overall accuracy. It is computed as (Jensen, 1996):

$$K = \frac{\sum\limits_{i=1}^{5} \frac{C_{ii}}{N} - \sum\limits_{i=1}^{5} \frac{C_{i*}C_{*i}}{N^2}}{1 - \sum\limits_{i=1}^{5} \frac{C_{i*}C_{*i}}{N^2}} \tag{13}$$

where C_{i*} is the sum of the elements along the i-th column and C_{*i} is the sum of the elements along the i-th row. The K coefficient has been interpreted according to Landis and Koch (1997), reported in Table 7.

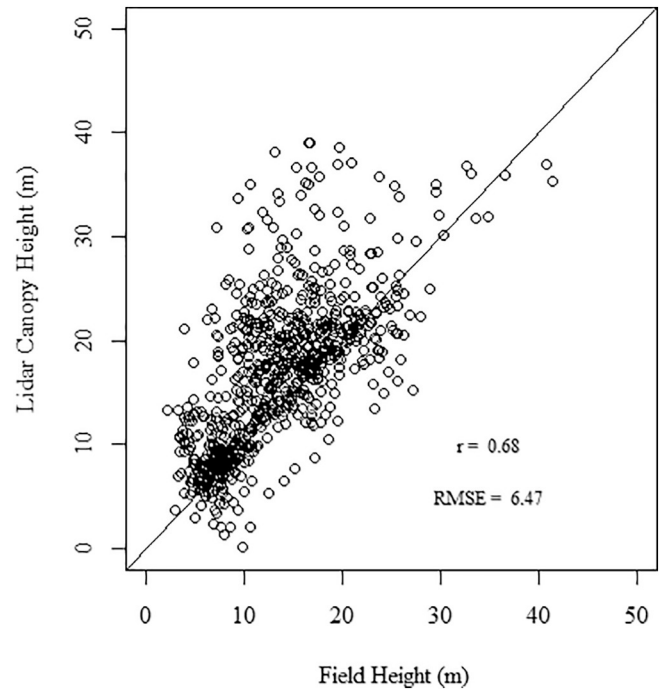To check the class separability, we computed the pairwise Jeffries-

Fig. 7. Scatterplot of the LiDAR CHM against tree heights measured in the field for 2013. Each point corresponds to a tree location in the field plots, for a total of 700 trees.

Matusita (JM) distance. The JM distance between well separated classes is above or equal to $\sqrt{2} = 1.41$ (Bruzzone et al., 1995) and varies between 0 and 2 (Matusita, 1966).
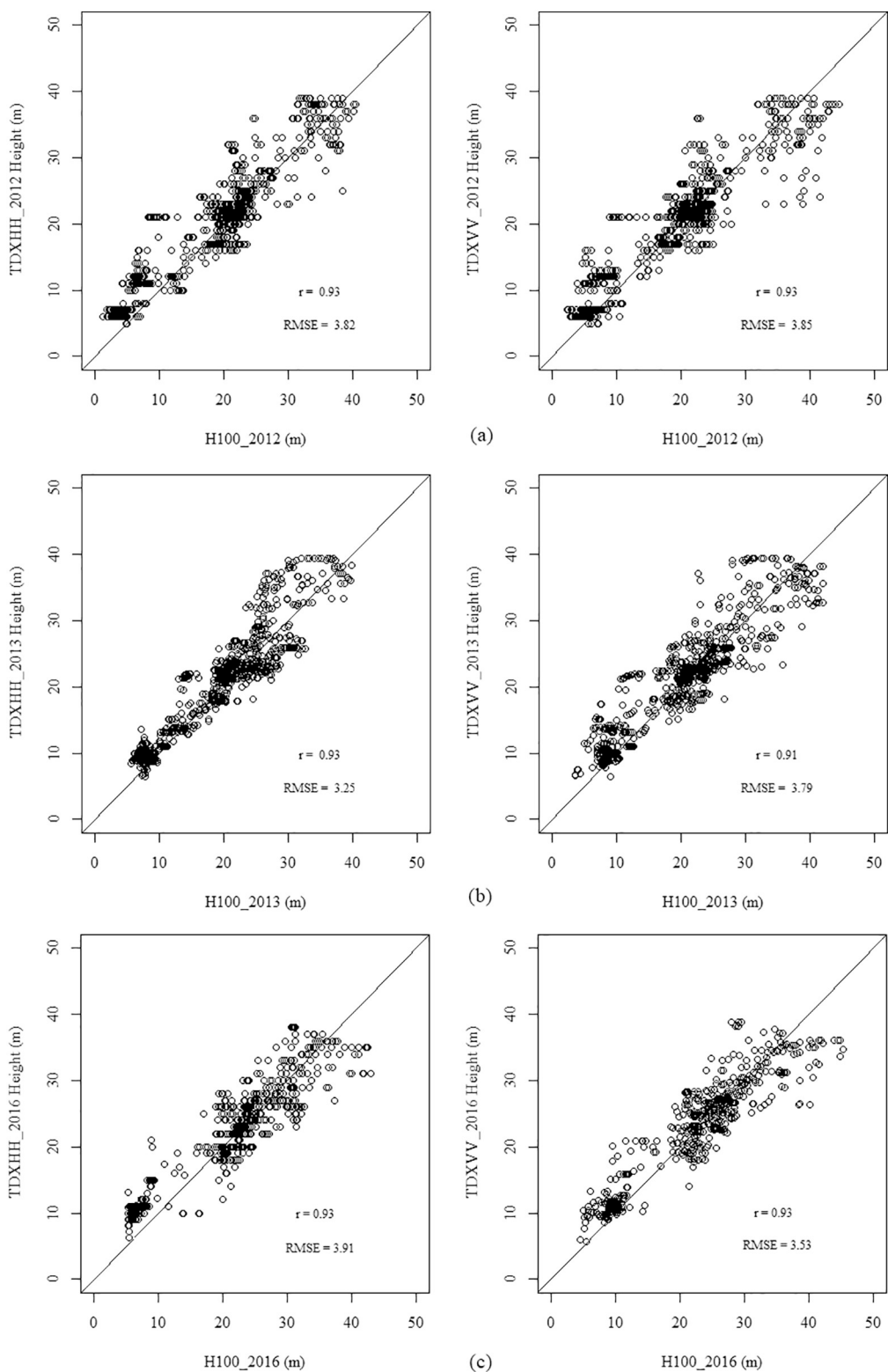
Fig. 8. Scatterplots of H100 against interferometric TanDEM-X heights at HH and VV polarization for 2012 (a), 2013 (b) and 2016 (c). Each point corresponds to a tree location in the field plots, for a total of 700 trees.

4. Results

4.1. Interferometric heights from TanDEM-X and H100

Fig. 6 shows the interferometric heights derived from TanDEM-X at HH polarization and the corresponding H100 from LiDAR for the years 2012, 2013 and 2016. The TanDEM-X height estimates have been obtained only over the LiDAR coverage where the ground topography is available. The high similarity between the TanDEM-X and H100 height maps is apparent. However, it is worth noting that some (large) discrepancies are still visible. It has been verified that they occur in areas affected by positive terrain slopes (i.e. facing the radar). In this case, the

Table 8
Class signatures generated from the training areas for 2012.

Classes 2012	Mean H100	Variance H100	Mean TDX[a]	Variance TDX[a]
OF	37.22	14.88	33.70	13.64
SFAdv	25.48	5.80	24.82	8.20
SFInt	15.66	3.61	15.40	6.24
SFIni	8.51	4.94	7.43	6.76
NF	2.03	2.56	2.35	2.05

[a] TDX interferometric forest height.

Table 9
Class signatures generated from the training areas for 2013.

Classes 2013	Mean H100	Variance H100	Mean TDX[a]	Variance TDX[a]
OF	37.09	14.99	34.88	13.40
SFAdv	25.60	4.90	25.66	9.04
SFInt	16.22	2.43	16.68	4.90
SFIni	9.48	2.27	9.55	8.94
NF	2.14	1.84	2.29	2.89

[a] TDX interferometric forest height.

Table 10
Class signatures generated from the training areas for 2016.

Classes 2016	Mean H100	Variance H100	Mean TDX[a]	Variance TDX[a]
OF	38.40	19.33	36.36	16.97
SFAdv	25.51	3.97	26.56	10.90
SFInt	16.59	2.70	15.40	8.85
SFIni	9.562	2.38	6.80	11.77
NF	1.027	0.97	5.26	6.07

[a] TDX interferometric forest height.

resulting (slope-corrected) vertical wavenumber is too large to allow for a meaningful inversion. In the 2016 acquisitions they occur also in flat areas, bare or with short stands. In this case some residual decorrelation contribution is still present, that is interpreted as a taller volume by the InSAR inversion, resulting in an overestimation of the volume height. However, the effect of this residual decorrelation is negligible in taller forested areas, because the total decorrelation is dominated by the volume decorrelation. This is confirmed by the analysis in Fig. 8.

Fig. 7 shows a scatterplot comparing the heights measured in the field in 2013 and the (top) LiDAR CHM height extracted at the 700 tree locations in the seven field plot and acquired in the same year. The correlation coefficients (r) and root-mean-square error (RMSE) are reported as well. There is a relevant, but not full, correlation between the field measurements and the LiDAR CHM with r = 68% and RMSE = 6.5 m. It is apparent from the scatterplot of Fig. 7 that the LiDAR CHM heights are larger than the heights measured on ground. This is essentially due to the difficulty of measuring top (tree) height on ground in dense forest environments.

Fig. 8 shows the validation of the interferometric height from TanDEM-X in HH and VV polarization for 2012, 2013 and 2016 against the LiDAR H100 at the selected tree locations, similar to Fig. 7. The comparison for HH polarization in the 3 years showed a high similarity

with r = 93% and RMSE between 3.25 m and 3.91 m, and for VV polarization r is between 91% and 93% and RMSE between 3.53 m and 3.85 m. The results were similar for both polarizations, and the interferometric height derived from TanDEM-X at HH polarization were selected for further analysis.

4.2. Classification of the successional stages and accuracy

The class signatures of the training samples for each of the 5 classes (OF, SFAdv, SFInt, SIni and NF) for the H100 and TanDEM-X heights for 2012, 2013 and 2016 are shown in Tables 8, 9 and 10. Between the years 2012, 2013 and 2016 the mean and variance was similar for each class. Analysing the Tables 8, 9 and 10 we note that amongst all the classes OF has the highest variance. This can be explained because OF is the most heterogeneous, most stratified forest type and includes emergent individual trees over the canopy. The lowest variance is found in the NF class.

When comparing the mean heights per class shown in Table 1 and Table 4, which are based on field measurements of the heights of individual trees, to the mean of each class of the training samples from Tables 8, 9 and 10, H100 and TanDEM-X interferometric heights are somewhat overestimated since these predominantly describe the forest top height volume. However, those datasets showed good results for classification purposes. This is corroborated by the Jeffries-Matusita (JM) distance shown in Table 11. The separability between the classes is good except for the class SFIni and NF of the TDX 2016 interferometric height (JM = 0.11). This can be explained by problems with the TanDEM-X interferometric height inversion for 2016 in NF areas of that image. The separability between the classes OF and SFAdv and between SFInt and SFIni was lower showing values between 1.18 and 1.40 for TDX interferometric heights. However, the JM distance generally shows a good separability between the classes with most of the values above 1.40 (Bruzzone et al., 1995) (Table 11).

For 2012, Fig. 9 shows the classification maps of the successional stages obtained by applying the ML classifier to the interferometric TanDEM-X heights (05/12/2012) at HH polarization and of H100 (31/07/2012). Visually, there is a high similarity between both classifications. This is confirmed by the confusion matrix and cross-validation reported in Table 12. The overall accuracy is 92% for the H100 classification and K = 0.90. For TanDEM-X heights, the overall accuracy is 87% and K = 0.84. In both classifications, the NF classes are unaffected by class confusion (100% of pixels classified correctly). For the classification of H100 some class confusion is found for SFIni (98% of pixels classified correctly) and OF (96% of pixels classified correctly) and the greatest confusion is found for SFAdv (87% of pixels classified correctly) and SFInt (83% of pixels classified correctly). For the classification of TanDEM-X height, the least confusion is found for OF (93% of pixels classified correctly) and the most confusion is found for SFInt (79% of pixels classified correctly) and SFAdv (84% of pixels classified correctly). The results show a slightly better performance of the classification using H100 heights rather than TanDEM-X heights.

For 2013, Fig. 10 shows the classification maps obtained with the interferometric TanDEM-X heights (30/05/2013) at HH polarization and the H100 (10/09/2013) heights. Visually they are very similar. The confusion matrix and cross-validation is shown in Table 13. For LiDAR
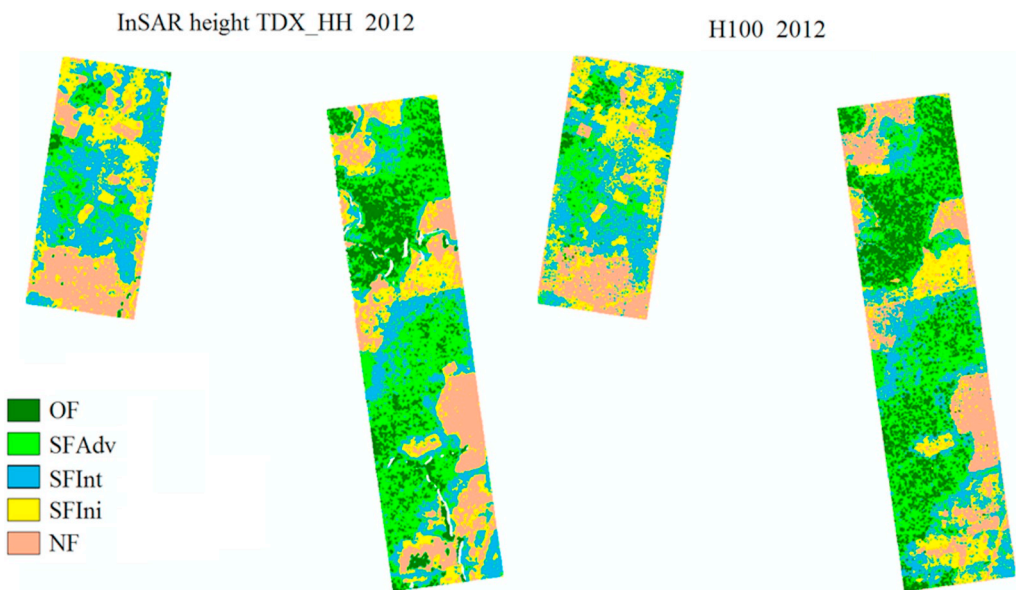
Table 11
Jeffries-Matusita Distance for the class combinations for each image.

Images	OF-SFAdv	OF-SFInt	OF-SFIni	OF-NF	SFAdv-SFInt	SFAdv-SFIni	SFAdv-NF	SFInt-SFIni	SFInt-NF	SFIni-NF
H100 2012	1.64	1.99	1.99	2.00	1.84	1.99	2.00	1.55	1.99	1.51
TDX 2012	1.20	1.97	1.99	2.00	1.57	1.98	1.99	1.40	1.98	1.11
H100 2013	1.64	1.99	1.99	2.00	1.90	1.99	2.00	1.82	1.99	1.92
TDX 2013	1.23	1.97	1.99	1.99	1.53	1.94	1.99	1.22	1.97	1.13
H100 2016	1.70	1.99	1.99	2.00	1.89	1.99	2.00	1.82	2.00	1.99
TDX 2016	1.16	1.97	1.99	1.99	1.58	1.97	1.99	1.18	1.67	0.11

InSAR height TDX_HH 2012

H100 2012

- ■ OF
- ■ SFAdv
- ■ SFInt
- ■ SFIni
- ■ NF

Fig. 9. Supervised classification of interferometric heights from TanDEM-X HH (05/12/2012) and LiDAR H100 (31/07/2012). The selected classes were old growth forest (OF), secondary forest in advanced stage (SFAdv), secondary forest in intermediary stage (SFInt), secondary forest in initial stage (SFIni) and non-forest (NF). The two rectangles correspond to the LiDAR coverage.

Table 12
Confusion matrix and cross-validation of TanDEM-X and H100 for 2012.

Classes	Ref. OF	Ref. SFAdv	Ref. SFInt	Ref. SFIni	Ref. NF
H100%					
OF	96	3	0	0	0
SFAdv	4	87	8	0	1
SFInt	0	10	83	1	0
SFIni	0	0	9	98	4
NF	0	0	0	1	95
	100	100	100	100	100
Overall Accuracy = 0.92; Kappa = 0.90					
TDX HH%					
OF	93	2	0	0	0
SFAdv	7	84	9	0	0
SFInt	0	14	79	6	0
SFIni	0	0	12	85	1
NF	0	0	0	9	99
	100	100	100	100	100
Overall Accuracy = 0.87; Kappa = 0.84					

Table 13
Confusion matrix and cross-validation of TanDEM-X and H100 for 2013.

Classes	Ref. OF	Ref. SFAdv	Ref. SFInt	Ref. SFIni	Ref NF
H100%					
OF	95	4	0	0	0
SFAdv	5	88	8	0	0
SFInt	0	8	84	1	0
SFIni	0	0	8	99	0
NF	0	0	0	0	100
100	100	100	100	100	100
Overall Accuracy = 0.93; Kappa = 0.91					
TDX HH%					
OF	93	5	0	0	0
SFAdv	7	82	8	0	0
SFInt	0	13	80	13	0
SFIni	0	0	12	80	0
NF	0	0	0	7	100
	100	100	100	100	100
Overall Accuracy = 0.87; Kappa = 0.84					

InSAR height TDX_HH 2013

H100 2013

- ■ OF
- ■ SFAdv
- ■ SFInt
- ■ SFIni
- ■ NF

Fig. 10. Supervised classification of interferometric height from TanDEM-X HH (30/05/2013) and H100 (10/09/2013). The selected classes were old growth forest (OF), secondary forest in advanced stage (SFAdv), secondary forest in intermediary stage (SFInt), secondary forest in initial stage (SFIni) and non-forest (NF). The two rectangles correspond to the LiDAR coverage.
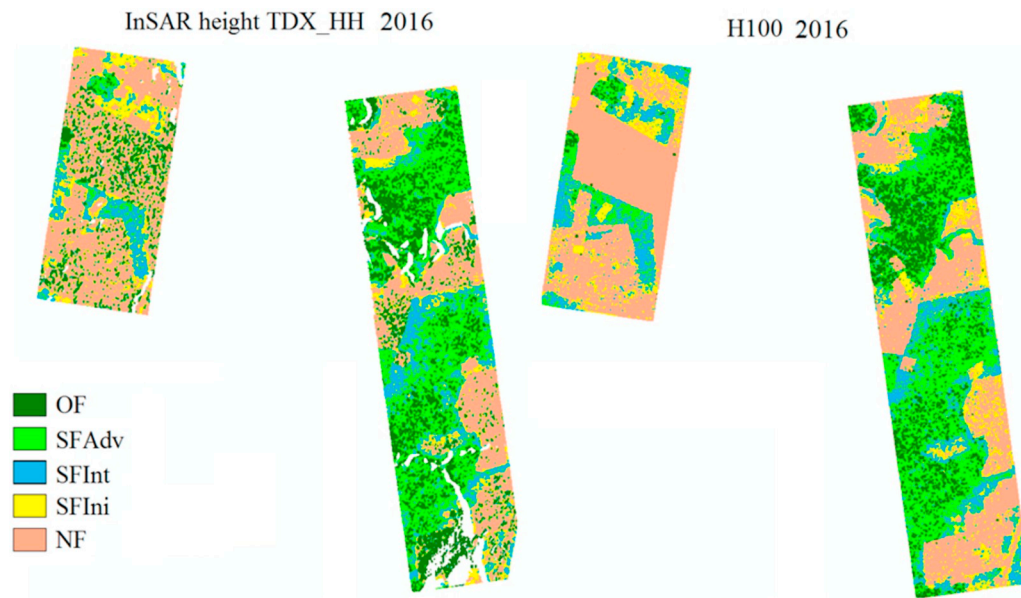
Table 14

Confusion matrix and cross-validation of TanDEM-X and H100 for 2016.

Classes	Ref. OF	Ref. SFAdv	Ref. SFInt	Ref. SFIni	Ref. NF
H100%					
OF	84	16	0	0	0
SFAdv	8	74	23	0	0
SFInt	7	10	64	3	0
SFIni	1	0	13	70	0
NF	0	0	0	27	100
	100	100	100	100	100
Overall Accuracy = 0.80; Kappa = 0.75					
TDX HH %					
OF	82	15	0	21	0
SFAdv	15	79	28	11	0
SFInt	3	6	46	11	0
SFIni	0	0	25	18	50
NF	0	0	1	39	50
	100	100	100	100	100
Overall Accuracy = 0.55; Kappa = 0.43					

H100, the overall accuracy is 93% and $K = 0.91$. For the TanDEM-X heights, the overall accuracy is 87% and $K = 0.84$. In both classifications, the NF classes are identified 100% correctly. For the H100 classification the lowest confusion was found for SFIni (99% of pixels classified correctly) and OF (95% of pixels classified correctly), and the greatest confusion was found for SFAdv (88% of pixels classified correctly) and SFInt (84% of pixels classified correctly). For TanDEM-X, the lowest confusion was found for OF (93% of pixels classified correctly) and SFAdv (82% of pixels classified correctly) the greatest confusion was found for SFInt (80% of pixels classified correctly) and SFIni (80% of pixels classified correctly). As for the 2012 classifications, the results for 2013 show a slightly better performance for the LiDAR H100 classification.

For 2016, Fig. 11 shows the classification maps obtained with the interferometric TanDEM-X height (23/01/2016) at HH polarization and the H100 heights (23/03/2016). Similarities between these two classification maps exist, especially for OF, SFAdv and SFInt. However, some confusion between SFIni and NF is apparent when comparing the H100 and TanDEM-X classifications. These misclassifications are mainly caused by the insufficiency of the inversion scheme to unambiguously identify bare soil and smaller tree stands, as already discussed when commenting Fig. 6. This is confirmed by the confusion matrix and cross-validation shown in Table 14. The overall accuracy is

80% for the H100 classification and $K = 0.75$. For TanDEM-X the overall accuracy is 55% and $K = 0.43$. For the H100 classification NF is 100% correctly classified, OF 84%, SFAdv 74%, SFIni 70% and SFInt 64% correctly classified. For the TanDEM-X classification, the lowest confusion is found for OF (82% of pixels classified correctly) and SFAdv (79% of pixels classified correctly) and the greatest confusion for SFIni (18% of pixels classified correctly), SFInt (46% of pixels classified correctly) and NF (50% of pixels classified correctly). As for 2012 and 2013, the results for 2016 show a better performance with the H100 classification than TanDEM-X. The TanDEM-X height underestimated SFIni and NF. Although the Table 14 does not show any confusion between OF and NF because there was no ground measurements in the confusion area for the validation, visually we observe a lot of class confusion in between NF areas and OF when the H100 and TanDEM-X interferometric heights for 2016 are compared.

5. Discussion

The LiDAR CHM top heights extracted at 700 tree locations have been compared to the corresponding tree heights measured in-situ. This comparison has shown a certain agreement. However, the LiDAR CHM heights tend to be larger than the heights measured from ground, and this discrepancy result in a RMSE of around 6.5 m. This uncertainty of the field plots in relation to LiDAR measurements is common in tropical areas due to the complexity of this ecosystem. First of all, trees adjacent to an inventory plot could extend their canopy into the plot. In this case, the height of those trees would be measured by a LiDAR, but not on the field. Furthermore, the geolocation of the ground measurement plot (and of the trees inside) is subject to some error which can result in a significant discrepancy when comparing the heights. Additionally, in multi-layered dense forest stands like the tropical ones the actual tree top height could be missed (not visible) from the ground, while it is seen and correctly measured from top by a (airborne) LiDAR instrument. All these factors may have contributed to an increased RMSE between the LiDAR CHM and the height measured from the field, the extent of which can however not be quantified.

A higher correlation (~0.93) and a lower RMSE (~3 m) has been found between the TanDEM-X forest heights and the LiDAR H100 calculated from the CHM, independently of the polarization channel. The TanDEM-X estimation performance worsened for short stands for the acquisition in 2016, most likely due to residual uncompensated non-volumetric decorrelation contributions. In general, the height

estimation performance obtained here is comparable to the one found in Kugler et al. (2014), where a correlation of 0.97 and a RMSE of 3 m was found for a tropical forest site in Mawas, Indonesia, using a single-pol inversion of forest heights at HH polarization in the rainy season. However, in Kugler et al. (2014) the estimation performance changes with seasonality. Such a variability has not been found here, where forest height has been inverted in both the wet (2012 and 2016) and the dry season (2013) with similar performance. In contrast, a similarity between the two studies is that the use of the LiDAR ground topography clearly contributed to the obtained satisfactory performance in such dense environments. Although it limited the coverage of the estimates, height estimation inaccuracy due to the limited X-band penetration in tropical forest stands could be overcome. To confirm this, a dual-pol forest height inversion was attempted in Tapajós with the 2012 data set. It has been found that there is not enough polarization diversity to allow a determined height inversion in more than the 50% of the pixels. Not only, but the reduced penetration introduced a non-negligible height underestimation.

The Tapajós National Forest region has been studied for decades as a supersite representative of the dense rainforest of the eastern Brazilian Amazon (Santos et al., 2003; Espírito-Santo et al., 2005; Espírito-Santo et al., 2014; Bispo et al., 2016; Silva et al., 2016; Cassol et al., 2019; Pôssa et al., 2018; Wiederkehr et al., 2019). Many studies have explored the successional forest stages of this area considering field measurements (Lu, 2005; Silva et al., 2016; Cassol et al., 2019) and also remote sensing datasets (Santos et al., 2003; Espírito-Santo et al., 2005; Galvão et al., 2009; Cassol et al., 2019; Pôssa et al., 2018; Wiederkehr et al., 2019). Table 4 with the local field data description used in this study is compatible with Table 1, which is based on a review by Lu (2005) using field inventory measurements also from other areas. Based on those evidences we assume that our training samples (Tables 5 and 6, Figs. 4 and 5) used in the classification are also representative for the eastern Amazon successional forests stages types with similar environmental conditions and anthropogenic impacts. The application of our methodology is conditional on the availability of a LiDAR DTM.

Considering the class signatures of the training samples (Tables 8, 9 and 10), the largest variance is in the class OF due to the high heterogeneity of this class in the TanDEM-X interferometric height images and H100. This high variance is expected due to the heterogeneity and high level of stratification of this forest type (Galvão et al., 2015; Berveglieri et al., 2016). This is also corroborated by the JM distance between the classes OF and SFAdv (Table 11). The JM distance between SFIni and NF and between OF and SFAdv showed less separability when compared to the other classes which can be explained by more overlap between the heights.

The results obtained by the maximum likelihood classification demonstrate that with the forest heights derived from TanDEM-X, it was possible to separate different successional stages. A total of five classes (OF, SFAdv, SFInt, SFIni and NF) were separated with an overall accuracy of 87%, for 2012 and 2013. The obtained accuracy is very close to the one obtained by using the LiDAR H100 heights. The residual uncompensated non-volumetric decorrelation contributions in the acquisition of 2016 made the overall accuracy decrease to 55%. High confusion between the classes SFIni (50% of pixels were classified correctly) and NF (50% of pixels were classified correctly) were found here. The classification accuracies for the classes OF and SFAdv were 82% and 79% respectively. It has also been verified that if just three classes, for example old growth forest, secondary forest and non-forest, are considered the classification accuracy increases to about 93%, 86%, 90% respectively. Such classification accuracies could be obtained thanks to the use of top heights, therefore constituting an improvement with respect to recent studies. For instance, De Grandi et al., 2016 found that by using the TanDEM-X phase centre height, i.e. the DEM, the separability between forest classes (primary or secondary forest) and non-forest (grassland) was high, while primary and secondary forest were more difficult to separate. This is due to the fact that the phase centre height contains information of the variability of the underlying topography, which is not separated from the canopy one. A wavelet decomposition could mitigate this effect by optimizing the scale of the wavelet function. By using forest top height, the effect of the ground topography could be entirely removed, although it still has an effect on the height inversion. Not only, but the successional stage separation could be obtained at the same resolution of the estimated heights. Nevertheless it is important to note that forest heights could be accurately estimated from TanDEM-X data only by using the external LiDAR ground topography.

The experiments presented here showed for the first time that the forest height derived from TanDEM-X can be used to separate tropical forest into different successional stages in tropical areas with an accuracy of about 80%. The resulting classification maps can be integrated into forest monitoring programmes at regional and national scale. Studies to classify tropical forest in different successional stages have been carried out for more than thirty years using images from passive and active sensors (Santos et al., 2003; Lu, 2005; Kuplich, 2006; Wijaya et al., 2010; Castilho et al., 2012; Carreiras et al., 2017). However, due the high heterogeneity, stratification and density, the classification of those different kinds of successional stages in large areas using remote sensing is still a challenge. Keeping in mind that forest height is one of the most important parameters to characterize tropical forest in different stages, an estimation of this variable with a good accuracy over large areas provides critical information.

6. Conclusion

The validation of TanDEM-X interferometric heights showed a high performance with a low uncertainty with respect to the LiDAR H100 height. The height estimation performance was found to be stable over time. It was shown for the first time that TanDEM-X interferometric heights combined with LiDAR ground topography can be used to identify different successional and/or disturbance forest stages even in dense tropical forest such as the Tapajós forest. Old-growth forest, secondary forest in different successional stages and non-forest could be distinguished.

Our results suggest that the approach described here allows to monitor the successional forest stages. Investigations are ongoing to confirm these capabilities in different tropical forest test sites, and to further assess the robustness of the methodology. The availability of an external (LiDAR) DTM, which often is not the case in other tropical regions, limits the use of this approach with TanDEM-X data and the coverage of the resulting classification maps. Alternative approaches that can rely on the TanDEM-X data only have started, see e.g. Pulella et al., 2017. Larger wavelengths would provide penetration until the ground, and therefore enable full-coverage height and classification maps. This could be the case for the L-band Tandem-L mission proposal.

References

Araújo, M.M., Tucker, J.M., Vasconcelos, S.S., Zarin, D.J., Oliveira, W., Sampaio, P.D., Rangel-Vasconcelos, L.D., Oliveira, F.A., Coelho, R.F.R., Aragão, D.V., Miranda, I., 2005. Padrão e processo sucessionais em florestas secundárias de diferentes idades na Amazônia Oriental. Ciência Florestal 15, 343–357.

Askne, J.I.H., Dammert, P.B.G., Ulander, L.M.H., Smith, G., 1997. C-band repeatpass interferometric SAR observations of the forest. IEEE Trans. Geosci. Remote Sensing. 35, 25–35.

Aslan, A., Rahman, A.F., Robeson, S.M., 2018. Investigating the use of Alos Prism data in detecting mangrove succession through canopy height estimation. Ecol. Indic. 87, 136–143.

Bamler, R., Hartl, P., 1998. Synthetic aperture radar interferometry. Inverse problems 14, R1–R54.

Banin, L., Feldpausch, T.R., Phillips, O.L., Baker, T.R., Lloyd, J., Affum-Baffoe, K., Arets, E.J.M.M., Berry, N.J., Bradford, M., Brienen, R.J.W., Davies, S., 2012. What controls tropical forest architecture? Testing environmental, structural and floristic drivers. Glob. Ecol. Biogeogr. 21 (12), 1179–1190.

Berveglieri, A., Tommaselli, A.M.G., Imai, N.N., Ribeiro, E.A.W., Guimaraes, R.B., Honkavaara, E., 2016. Identification of successional stages and cover changes of tropical forest based on digital surface model analysis. IEEE Journal of Selected Topics in Applied Earth Observations and Remote Sensing 9 (12), 5385–5397.

Bispo, P.C., Santos, J.R., Valeriano, M.M., Touzi, R., Seifert, F.M., 2014. Integration of polarimetric PALSAR attributes and local geomorphometric variables derived from SRTM for forest biomass modeling in central Amazonia. Can. J. Remote Sens. 40 (1), 26–42.

Bispo, P.C., Santos, J.R., Valeriano, M.M., Graça, P.M.L.A., Balzter, H., França, H., Bispo, P.C., 2016. Predictive models of primary tropical forest structure from geomorphometric variables based on SRTM in the Tapajós region, Brazilian Amazon. PLoS One 11 (4), e0152009.

Brasil, 2012. *Lei n° 12.678, de 25 de junho de 2012.* Dispõe sobre alterações nos limites dos Parques Nacionais da Amazônia, dos Campos Amazônicos e Mapinguari, das Florestas Nacionais de Itaituba I, Itaituba II e do Crepori e da Área de Proteção Ambiental do Tapajós; altera a Lei no 12.249, de 11 de junho de 2010; e dá outras providências. Avaliabe in. http://www.planalto.gov.br/ccivil_03/_Ato2011-2014/2012/Lei/L12678.htm>, Accessed date: 10 August 2017.

Bruzzone, L., Roli, F., Serpico, B., 1995. An extension of the Jeffreys-Matusita distance to multiclass cases for feature selection. IEEE Trans. Geosci. Remote Sens. (6), 1318–1321.

Caicoya, A.T., Kugler, F., Hajnsek, I., Papathanassiou, K.P., 2016. Large-scale biomass classification in boreal forests with TanDEM-X data. IEEE Trans. Geosci. Remote Sens. 54, 5935–5951.

Carreiras, J.M.B., Jones, J., Lucas, R.M., Shimabukuro, Y.E., 2017. Mapping major land cover types and retrieving the age of secondary forests in the Brazilian Amazon by combining single-date optical and radar remote sensing data. Remote Sens. Environ. 194, 16–32.

Cassol, H.L.G., Carreiras, J.M.D.B., Moraes, E.C., Silva, C.V.D.J., Quegan, S., Shimabukuro, Y.E., 2019. Retrieving secondary forest aboveground biomass from polarimetric ALOS-2 PALSAR-2 data in the Brazilian Amazon. Remote Sens. 11 (1), 59.

Castilho, C., Rivard, B., Sánchez-Azofeifa, A., Calvo-Alvarado, J., Dubayah, R., 2012. LiDAR remote sensing for secondary tropical dry forest identification. Remote Sens. Environ. 121, 132–143.

Chazdon, R.L., Letcher, S.G., Van Breugel, M., Martínez-Ramos, M., Bongers, F., Finegan, B., 2007. Rates of change in tree communities of secondary neotropical forests following major disturbances. Philos. Trans. R. Soc. Lond. Ser. B Biol. Sci. 362, 273–289.

Chokkalingam, U., De Jong, W., 2001. Secondary Forest: A Working Definition and Typology. The International Forestry Review, pp. 19–26.

Cloude, S.R., Papathanassiou, K.P., 1998. Polarimetric SAR interferometry. IEEE Trans. Geosci. Remote Sens. 36, 1551–1565.

Cloude, S., Papathanassiou, K., 2003. Three-stage inversion process for polarimetric SAR interferometry. IEEE Proceedings-Radar, Sonar and Navigation 150, 125–134.

Cloude, S.R., Chen, H., Goodenough, D.G., 2013. Forest height estimation and validation using Tandem-X polinsar. In: Geoscience and Remote Sensing Symposium (IGARSS), pp. 1889–1892.

De Grandi, E.C., Mitchard, E., 2016. Tropical forest heterogeneity from TanDEM-X InSAR and LiDAR observations in Indonesia. In: SPIE Remote Sensing. International Society for Optics and Photonics, pp. 1000305–1000310.

De Grandi, E.C., Mitchard, E., Hoekman, D., 2016. Wavelet based analysis of TanDEM-X and LiDAR DEMs across a tropical vegetation heterogeneity gradient driven by fire disturbance in Indonesia. Remote Sens. 8, 641.

Espírito-Santo, F.D.B., Shimabukuro, Y.E., Aragão, L.E.O.C., Machado, E.L., 2005. Análise da composição florística e fitossociológica da floresta nacional do Tapajós com o apoio geográfico de imagens de satélites. Acta Amazon. 35 (2), 155–173.

Espírito-Santo, F.D., Gloor, M., Keller, M., Malhi, Y., Saatchi, S., Nelson, B., Junior, R.C.O., Pereira, C., Lloyd, J., Frolking, S., Palace, M., 2014. Size and frequency of natural forest disturbances and the Amazon forest carbon balance. Nat. Commun. 5, 3434.

Feldpausch, T.R., Banin, L., Phillips, O.L., Baker, T.R., Lewis, S.L., Quesada, C.A., Affum-Baffoe, K., Arets, E.J., Berry, N.J., Bird, M., Brondizio, E.S., 2011. Height-diameter allometry of tropical forest trees. Biogeosci. Discuss. 7, 7727–7793.

Feldpausch, T.R., Lloyd, J., Lewis, S.L., Brienen, R.J., Gloor, M., Monteagudo Mendoza, A., Lopez-Gonzalez, G., Banin, L., Abu Salim, K., Affum-Baffoe, K., Alexiades, M., 2012. Tree height integrated into pantropical forest biomass estimates. Biogeosciences 9, 3381–3403.

Galvão, L.N.S., Ponzoni, F.V.J., Liesenberg, V., Santos, J.O.R.D., 2009. Possibilities of discriminating tropical secondary succession in Amazonia using hyperspectral and multiangular CHRIS/PROBA data. International Journal of Applied Earth Observations and Geoinformation 11 (1), 8–14.

Galvão, L.S., dos Santos, J.R., da Silva, R.D.A., da Silva, C.V., Moura, Y.M., Breunig, F.M., 2015. Following a site-specific secondary succession in the Amazon using the Landsat CDR product and field inventory data. Int. J. Remote Sens. 36 (2), 574–596.

Garestier, F., Dubois-Fernandez, P.C., Papathanassiou, K.P., 2008. Pine forest height inversion using single-pass X-band PolInSAR data. IEEE Trans. Geosci. Remote Sens. 46, 59–68.

Hajnsek, I., Kugler, F., Lee, S.K., Papathanassiou, K.P., 2009. Tropical-forest-parameter estimation by means of pol-InSAR: the INDREX-II campaign. IEEE Trans. Geosci. Remote Sens. 47, 481–493.

Jensen, J.R., 1996. Introductory Digital Image Processing A Remote Sensing Perspective, 2nd edition. Prentice Hall, Inc, Upper Saddle River, NJ.

Khati, U., Singh, G., Ferro-Famil, L., 2017. Analysis of seasonal effects on forest parameter estimation of Indian deciduous forest using TerraSAR-X PolInSAR acquisitions. Remote Sens. Environ. 199, 265–276.

Khati, U., Singh, G., Kumar, S., 2018. Potential of space-borne PolInSAR for forest canopy height estimation over India - a case study using fully polarimetric L-, C-, and X-Band SAR data. IEEE Journal of Selected Topics in Applied Earth Observations and Remote Sensing 11 (7), 2406–2416.

Kugler, F., Schulze, D., Hajnsek, I., Pretzsch, H., Papathanassiou, K.P., 2014. TanDEM-X pol-InSAR performance for forest height estimation. IEEE Trans. Geosci. Remote Sens. 52, 6404–6422.

Kugler, F., Lee, S., Hajnsek, I., Papathanassiou, K., 2015. Forest height estimation by means of pol-InSAR data inversion: the role of the vertical wavenumber. IEEE Trans. Geosci. Remote Sens. 53, 5294–5311.

Kuplich, T.M., 2006. Classifying regenerating forest stages in Amazônia using remotely sensed images and a neural network. For. Ecol. Manag. 234, 1–3): 1–9.

Van Laar, A., Akça, A., 2007. Forest mensuration. First ed., Springer Science & Business Media. The Netherlands.

Lagomasino, D., Fatoyinbo, T., Lee, S., Feliciano, E., Trettin, C., Simard, M., 2016. A comparison of mangrove canopy height using multiple independent measurements from land, air, and space. Remote Sens. 8, 327.

Landis, J.R., Koch, G.G., 1997. The measurement of observer agreement for categorical data. Biometrics 1, 159–174.

Lee, S.K., Kugler, F., Papathanassiou, K., Moreira, A., 2009. Forest height estimation by means of pol-InSAR limitations posed by temporal decorrelation. In: 11th ALOS Kyoto & Carbon Initiative, Tsukuba, Japan.

Lee, S., Kugler, F., Papathanassiou, K., Hajnsek, I., 2013. Quantification of temporal decorrelation effects at L-band for polarimetric SAR interferometry applications. IEEE J. Sel. Topics Appl. Earth Obs. Remote Sens. 1351–1367.

Lei, Y., Treuhaft, R., Keller, M., Santos, M.N., Gonçalves, F., Neumann, M., 2018. Quantification of selective logging in tropical forest with spaceborne SAR interferometry. Remote Sens. Environ. 211, 167–183.

Lu, D., 2005. Integration of vegetation inventory data and Landsat TM image for vegetation classification in the western Brazilian Amazon. For. Ecol. Manag. 213 (1–3), 369–383.

Lu, D., Mausel, P., Brondízio, E., Moran, E., 2003. Classification of successional forest stages in the Brazilian Amazon basin. For. Ecol. Manag. 181, 301–312.

Martins, F.D.S.R.V., dos Santos, J.R., Galvão, L.S., Xaud, H.A.M., 2016. Sensitivity of ALOS/PALSAR imagery to forest degradation by fire in Northern Amazon. Int. J. Appl. Earth Obs. Geoinf. 49, 163–174.

Matusita, K., 1966. A distance and related statistics in multivariate analysis. In: Krishnaiah, P.R. (Ed.), Multivariate Analysis. Academic Press, New York, pp. 187–200.

McGaughey, R.J., 2014. Manual FUSION/LDV Software for LiDAR Data Analysis and Visualization. US Department of Agriculture, Forest Service (Version 3.42).

Mesquita, R.C.G., Ickes, K., Ganade, G., Williamson, G.B., 2001. Alternative successional pathways in the Amazon Basin. J. Ecol. 89, 528–537.

Moran, E.F., Brondizio, E.S., 1998. Land-use change after defor-estation in Amazonia. In: Liverman, D., Moran, E.F., Rindfuss, R.R., Stern, P.C. (Eds.), People and Pixels: Linking Remote Sensing and Social Science. National Academy Press, Washing-ton, DC, pp. 94–120.

Naesset, E., Ørka, H.O., Solberg, S., Bollandsås, O.M., Hansen, E.H., Mauya, E., Zahabu, E., Malimbwi, R., Chamuya, N., Olsson, H., Gobakken, T., 2016. Mapping and estimating forest area and aboveground biomass in miombo woodlands in Tanzania using data from airborne laser scanning, TanDEM-X, RapidEye, and global forest maps: a comparison of estimated precision. Remote Sens. Environ. 175, 282–300.

Nyirambangutse, B., Zibera, E., Uwizeye, F.K., Nsabimana, D., Bizuru, E., Pleijel, H., Uddling, J., Wallin, G., 2017. Carbon stocks and dynamics at different successional stages in an Afromontane tropical forest. Biogeosciences 14, 1285.

Olesk, A., Voormasik, K., Vain, A., Noorma, M., Praks, J., 2015. Seasonal differences in forest height estimation from interferometric TanDEM-X coherence data. IEEE J. Sel. Topics Appl. Earth Obs. Remote Sens. 8, 5565–5572.

Papathanassiou, K., Cloude, S.R., 2001. Single-baseline polarimetric SAR interferometry. IEEE Trans. Geosci. Remote Sens. 39, 2352–2363.

Pavanelli, J.A.P., Santos, J.R.D., Galvão, L.S., Xaud, M., Xaud, H.A.M., 2018. PALSAR-2/ALOS-2 and OLI/LANDSAT-8 data integration for land use and land cover mapping in Northern Brazilian Amazon. Boletim de Ciências Geodésicas 24 (2), 250–269.

Pôssa, E.M., Gama, F.F., Santos, J.R., Mura, J.C., Bispo, P.C., 2018. Análise de uso e cobertura da terra na região do tapajós, Amazônia central, a partir de dado polarimétrico PALSAR/ALOS-1 e coerência interferométrica TanDEM-X. Revista Brasileira de Geografia Física 11 (06), 2094–2108.

Pulella, A., Bispo, P.C., Pardini, M., Kugler, F., Cazcarra, V., Tello, M., Papathanassiou, K.,

Balzter, H., Rizaev, I., Santos, M.N., dos Santos, J.R., 2017. Tropical forest structure observation with TanDEM-X data. In: IEEE International Geoscience and Remote Sensing Symposium (IGARSS*)*, pp. 918–921.

Qi, W., Dubayah, R.O., 2016. Combining TanDEM-X InSAR and simulated GEDI lidar observations for forest structure mapping. Remote Sens. Environ. 187, 253–266.

Richards, J.A., Xiuping, J., 2006. Remote Sensing Digital Image Analysis. Springer-Verlag, Berlin Heidelberg.

Ricklefs, R.E., Relyea, R., 2008. The Economy of Nature, Seventh ed. W.H. Freeman and Company, New York.

Sadeghi, Y., St-Onge, B., Leblon, B., Simard, M., 2016. Canopy height model (CHM) derived from a TanDEM-X InSAR DSM and an airborne lidar DTM in boreal forest. IEEE J. Sel. Topics Appl. Earth Obs. Remote Sens. 9, 381–397.

Salomão, R.D.P., Vieira, I.C.G., Júnior, S.B., Amaral, D.D., Santana, A.C., 2012. Sistema Capoeira Classe. Uma proposta de sistema de classificação de estágios sucessionais de florestas secundárias para o estado do Pará. Boletim Museu Paraense Emílio Goeldi de Ciencias Naturais 7, 297–317.

Santos, J.R., Freitas, C.C., Spinelli- Araujo, L., Dutra, L.V., Mura, J.C., Gama, F.F., Soler, L. S., Sant'Anna, S.J.S., 2003. Airborne P-band SAR applied to the aboveground biomass studies in the Brazilian tropical rainforest. Remote Sens. Environ., 87(4): 482–493.

Schlund, M., von Poncet, F., Hoekman, D.H., Kuntz, S., Schmullius, C., 2014. Importance of bistatic SAR features from TanDEM-X for forest mapping and monitoring. Remote Sens. Environ. 151, 16–26.

Schlund, M., von Poncet, F., Kuntz, S., Schmullius, C., Hoekman, D.H., 2015. TanDEM-X data for aboveground biomass retrieval in a tropical peat swamp forest. Remote Sens. Environ. 158, 255–266.

Silva, C.V.D.J., Santos, J.R.D., Galvão, L.S., Silva, R.D.A.D., Moura, Y.M., 2016. Floristic and structure of an Amazonian primary forest and a chronosequence of secondary succession. Acta Amazon. 46 (2), 133–150.

Silver, W.L., Neff, J., McGroddy, M., Veldkamp, E., Keller, M., Cosme, R., 2000. Effects of soil texture on belowground carbon and nutrient storage in a lowland Amazonian forest ecosystem. Ecosystems 3, 193–209.

Soja, M.J., Persson, H.J., Ulander, L.M.H., 2018. Modeling and detection of deforestation and forest growth in multitemporal TanDEM-X data. IEEE J. Sel. Topics Appl. Earth Obs. Remote Sens. 11, 3548–3563.

Treuhaft, R.N., Siqueira, P.R., 2000. Vertical structure of vegetated land surfaces from interferometric and polarimetric radar. Radio Sci. 35 (1), 141–177.

Treuhaft, R.N., Madsen, S.N., Moghaddam, M., van Zyl, J.J., 1996. Vegetation characteristics and underlying topography from interferometric radar. Radio Sci. 31 (6), 1449–1485.

Treuhaft, R.N., Gonçalves, F.G., dos Santos, J.R., Keller, M., Palace, M., Madsen, S., Sullivan, F., Graça, P., 2015. Tropical-forest biomass estimation at X-band from the spaceborne TanDEM-X interferometer. IEEE Geosci.Remote Sens. Lett. 12, 239–243.

Treuhaft, R., Lei, Y., Gonçalves, F., Keller, M., Santos, J.R., Neumann, M., Almeida, A., 2017. Tropical-forest structure and biomass dynamics from TanDEM-X radar interferometry. Forests 8, 277.

Vieira, I.C.G., Gardner, T.A., 2012. Florestas Secundárias tropicais: Ecologia e importância em paisagens antrópicas. Bol. Mus. Para. Emílio Goeldi. Cienc. Nat. 7 (3), 191–194.

Vieira, I.C.G., de Almeida, A.S., Davidson, E.A., Stone, T.A., de Carvalho, C.J.R., Guerrero, J.B., 2003. Classifying successional forests using Landsat spectral properties and ecological characteristics in eastern Amazonia. Remote Sens. Environ. 87, 470–481.

Wiederkehr, N.C., Gamma, F.F., Santos, J.R., Mura, J.C., Bispo, P.C., Sano, E.E., 2019. Analysis of the target decomposition technique attributes and polarimetric ratios to discriminate land use and land cover classes of the Tapajós Region. Bulletin of Geodetic Sciences 25 (1), e2019002.

Wijaya, A., Liesenberg, V., Gloaguen, R., 2010. Retrieval of forest attributes in complex successional forests of Central Indonesia: Modelling and estimation of bitemporal data. For. Ecol. Manag. 259 (12), 2315–2326.

Zebker, H.A., Villasenor, J., 1992. Decorrelation in interferometric radar echoes. IEEE Trans. Geosci. Remote Sens. 30 (5), 950–959.